Research Article

The Identification Nanoparticle Sensor Using Back Propagation Neural Network Optimized by Genetic Algorithm

Yiwen Hu [1], **Ashutosh Sharma** [2], **Gaurav Dhiman** [3], **and Mohammad Shabaz** [4]

[1]*Testing Center of Aviation Theory, Civil Aviation Flight University of China Guanghan, Sichuan 618307, China*
[2]*Institute of Computer Technology and Information Security, Southern Federal University, Russia*
[3]*Government Bikram College of Commerce, Punjab, India*
[4]*Arba Minch University, Ethiopia*

Correspondence should be addressed to Yiwen Hu; yiwenhu21@outlook.com
and Mohammad Shabaz; mohammad.shabaz@amu.edu.et

This study draws attention towards the application of identification nanoparticle (NPs) sensor based on back propagation (BP) neural network optimized by genetic algorithm (GA) in the early diagnosis of cancer cells. In this study, the traditional and optimized BP neural networks are compared in terms of error between the actual value and the predictive value, and they are further applied to the NP sensor for early diagnosis of cancer cells. The results show that the root mean square (RMS) and mean absolute error (MAE) of the optimized BP neural network are comparatively much smaller than the traditional ones. The particle size of silicon-coated fluorescent NPs is about 105 nm, and the relative fluorescence intensity of silicon-coated fluorescent NPs decreases slightly, maintaining the accuracy value above 80%. In the fluorescence imaging, it is found that there is obvious green fluorescence on the surface of the cancer cells, and the cancer cells still emit bright green fluorescence under the dark-field conditions. In this study, a phenolic resin polymer CMK-2 with a large surface area is successfully combined with Au. NPs with good dielectric property and bioaffinity are selectively bonded to the modified electrode through a sulfur-gold bond to prepare NP sensor. The sensor shows good stability, selectivity, and anti-interference property, providing a new method for the detection of early cancer cells.

1. Introduction

In the past few years, people's increasingly high requirements for microscopic detection technology have led to an evolution, in the applications of various nanomaterials in the biological field. NPs refer to particles with a particle size between 1 and 100 nm, and it is a new material for research at the molecular level, cellular level, and subcellular level [1]. The NP-based nanotechnology can be applied to the diagnosis and treatment of tumors [2].

Fluorophores can be added to NPs by covalent bonding or embedding to form fluorescent NPs [3], which are used as fluorescent dyes for detection or labeling. Compared with ordinary fluorescent dyes, fluorescent NPs have high brightness, good stability, strong water solubility, and good biocompatibility [4]. Cancer cell imaging is of great significance in the diagnosis of tumors. As a carrier material, fluorescent NPs can enhance biological signals to facilitate detection [5]. Hyaluronic acid (HA) has a good application prospect in the diagnosis and treatment of tumor diseases [6]. A nanodrug-carrying system prepared by combining NPs and HA can specifically bind to receptor proteins on the cell surface to detect cancer cells. Shen et al. [7] prepared diamine-hyaluronic acid-iron-modified rhodamine fluorescent NPs for cancer imaging detection. The results proved that fluorescent NPs had high sensitivity and stability.

Sensors play an important role in various fields, and chemical sensors are generally used to detect chemical substances. Electrochemical biosensors use active substances in organisms as sensitive elements. It converts them into electrochemical signals to output characteristic signals such as potential, current, and capacitance [8]. The principle of
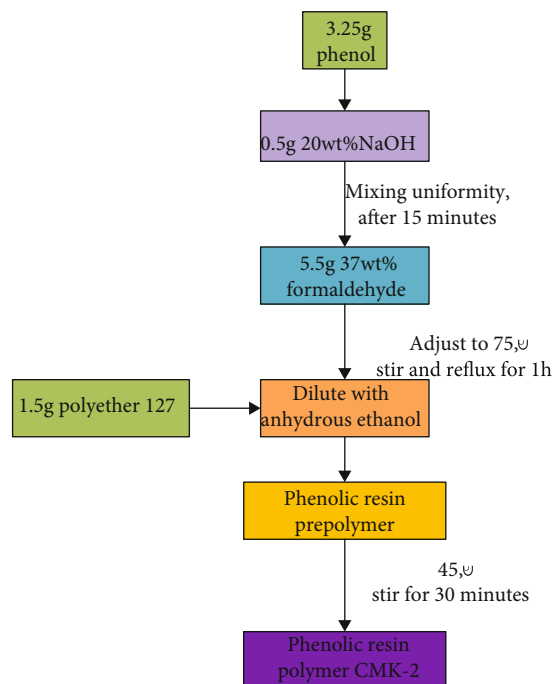
Figure 1: Preparation of CMK-2.

Figure 2: The preparation of Me-β-Cy/Au NPs/CMK-2/GCE.

Figure 3: The BP neural network.

electrochemical biosensor is as follows. When the active substance in the organism diffuses to the biosensitive layer, relevant chemical reactions occur. The biological signals are then converted into electrical signals that can be quantitatively analyzed. Finally, the concentration of the active substance can be identified by processing the electrical signals [9]. Nanomaterials have many functions in electrochemical sensors. They can modify electrodes, accelerate the rate of electron transfer, promote catalytic reactions, and immobilize biomolecules. They can further be used as carriers for markers, control switches for chemical reactions, as well as reactants [10]. The introduction of NPs into electrochemical biosensors can effectively improve its sensitivity and reproducibility.

The genetic algorithm (GA) is a probabilistic adaptive iterative algorithm that can process the discontinuous function through the global search [11], as it finds the global optimal solution by not being affected by gradient information. It can be used to optimize BP network [12]. When the optimized BP neural network based on GA is applied to the NP sensor, it endows the nanoparticle sensor with ideal stability by adjusting the weight and threshold [13].

In the past studies depicted in this section, it is revealed that alone neural network-based approaches do not provides satisfactory outcomes for finding optimal global solution for diagnosis of cancer cells and this is a great research challenge. In the study, the GA is used to optimize the BP neural network. The fluorescent NPs are applied in electrochemical sensors, with their basic characteristics expounded. The modified electrodes of Me-β-Cy/Au NPs/CMK-2/GCE are introduced in the biosensor which is applied in the early diagnosis of cancer cells, aimed at exploring the diagnostic value of fluorescent NP sensors for cancer cells.
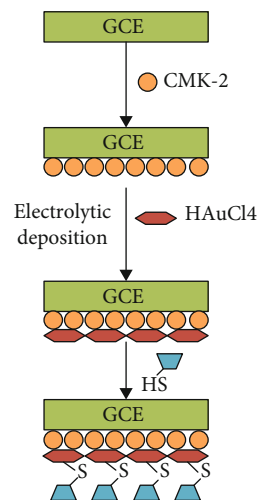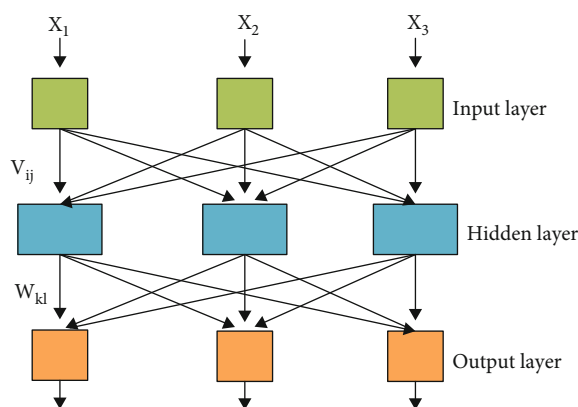
2. Experimental Methodology

2.1. Me-β-Cy/Au NPs/CMK-2/GCE Electrodes

2.1.1. Preparation of CMK-2

(1) Preparation of the Phenolic Resin Prepolymer. 3.25 g of phenol is dissolved in 0.5 g of 20 wt% NaOH solution. 15 minutes later, the uniform mixture is slowly dripped into 5.5 g of 37 wt% formaldehyde solution, with the temperature adjusted to 75°C, followed by reflux for 1 h. After the mixture cools to 25°C, 0.4 mol/L HCl is used to adjust pH = 7, followed by evaporation treatment. The mixture is then diluted with absolute ethanol. After the white particles of NaCl are removed by filtering, the remaining light-yellow solution is the phenolic resin prepolymer.

(2) Preparation of CMK-2. 1.5 g of polyether F127 is added to the solution prepared above, with the temperature adjusted to 45°C, followed by stirring for 30 min to form a light-yellow transparent solution. The mixture is then transferred to a petri dish at 45°C and dried for 8 hours to remove ethanol. The temperature is adjusted again to 100°C for thermal polymerization for 24 hours to form the transparent film,
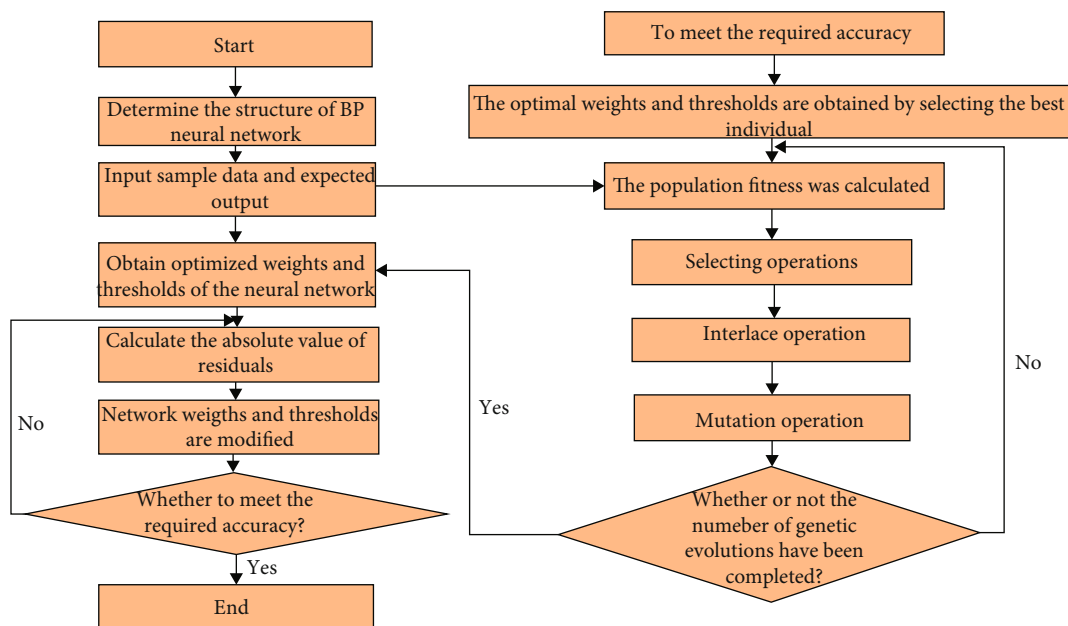
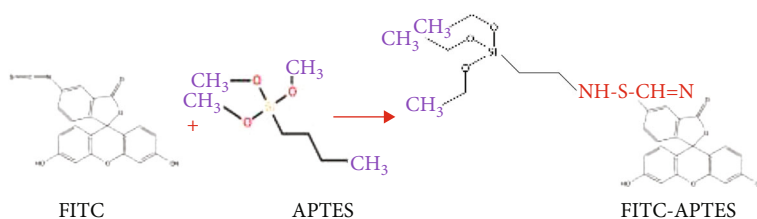Figure 4: The optimization of the BP neural network by GA.

Figure 5: The preparation of FITC-APTES.

which is pulverized and fired at 350°C for 5 hours under nitrogen conditions to finally obtain dark brown powder. The powder is then dispersed in 98% concentrated sulfuric acid solution, followed by reflux for 24 hours. After the template polyether F127 is removed, CMK-2 is finally obtained, as shown in Figure 1.

2.1.2. Preparation of Modified Electrode.

The glassy carbon electrode (GCE) is polished with $0.2\,\mu m$ and $0.05\,\mu m$ alumina wet powder, respectively, and then undergoes ultrasonic cleaning in absolute ethanol and ultrapure water, respectively. The control volume (CV) method is used for scanning activation in a 5 mmol/L sulfuric acid solution [14], with potential controlled at -0.5-1.6 V, and the scanning rate set as 100 mV/s. The electrode is then cleaned with ultrapure water and dried at room temperature.

1.8 mg of CMK-2 powder prepared above is dissolve in 1 mL of dimethylformamide (DMF), followed by ultrasound treatment for 1 h to form a uniformly dispersed black suspension. Subsequently, $2.5\,\mu L$ of the suspension is applied to bare GCE, dried at room temperature, and recorded as a CMK-2/GCE electrode [15]. The above electrode is placed in 0.6 mmol/L chloroauric acid (HAuCl$_4$) (Sigma-Aldrich, USA) solution for electrodepositing gold (Au NPs), with potential controlled at -0.5-1.6 V. The CV method is used
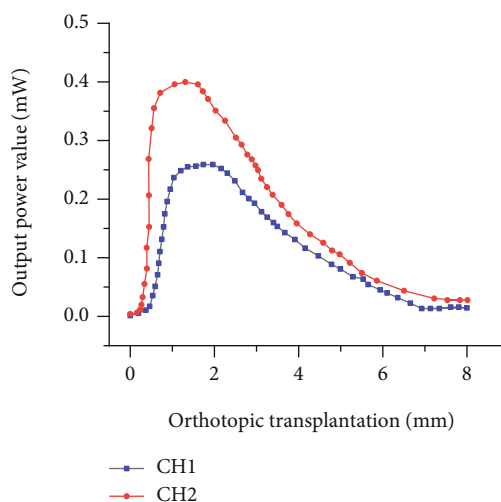

Figure 6: The relationship between displacement and received power.

to scan 10 times, with the scanning speed set as 50 mV/s, followed by rinse step using ultrapure water. It is then dried at room temperature and recorded as Au NPs/CMK-2/GCE. The above electrode is immersed in a phosphate buffer solution containing 1 mmol/L Me-β-Cy (Binzhou Zhiyuan
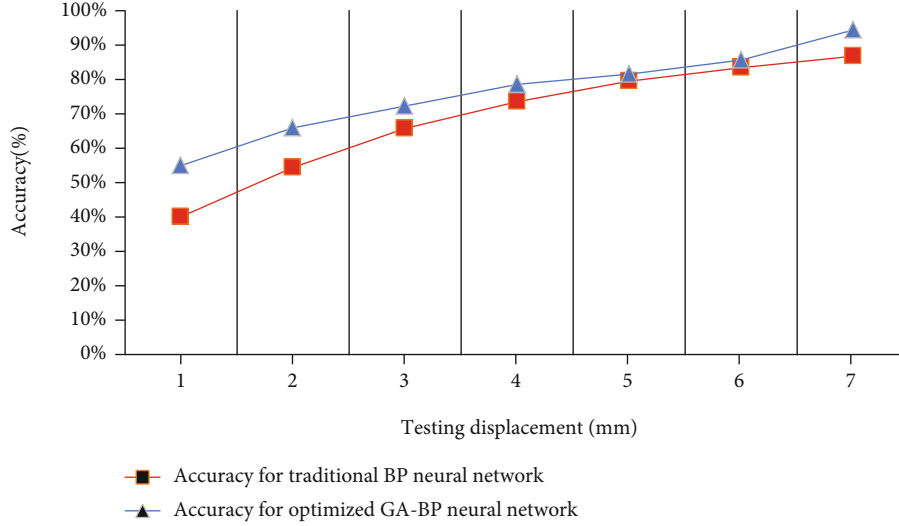
FIGURE 7: Accuracy values for traditional and optimized GA-BP neural networks.

Biotechnology, China) for assembling for 12 h, followed by rinse with ultrapure water. It is then dried at room temperature [16], denoted as Me-β-Cy/Au NPs/CMK-2/GCE, as shown in Figure 2.

2.2. The BP Neural Network Improved by GA. The BP neural network is a kind of feedforward neural network [17]. It is generally composed of an input layer, a hidden layer, and an output layer (Figure 3). The BP neural network has good self-learning and self-adaptation capabilities and strong fault tolerance [18].

In the study, the GA is used to optimize the initial weight threshold of the BP neural network, with the general initial weight search replaced by global search, so that the BP algorithm can accurately debug the neural network in the solution space, and search for the global optimal solution [19]. The optimization includes population initialization, fitness function selection, selection operation, crossover operation, and mutation operation [20], as shown in Figure 4.

After the training of the BP neural network, the sum of the residual absolute value between the predicted output and the expected output is set as the fitness function H.

$$H = l\left(\sum_{j=1}^{m}\left|y_j - p_j\right|\right), \text{where } y_j \neq p_j, \tag{1}$$

where l represents the coefficient, and it is 1 in the study. m represents the value of the output node, y_j represents the expected output value of the j point, and p_j represents the predicted output value of the j point. The probability of each individual is expressed as follows:

$$P_j = H\sum_{j=1}^{M} H_j, \tag{2}$$

where H represents the fitness function and P_j represents the probability of an individual j. In this study, the real number
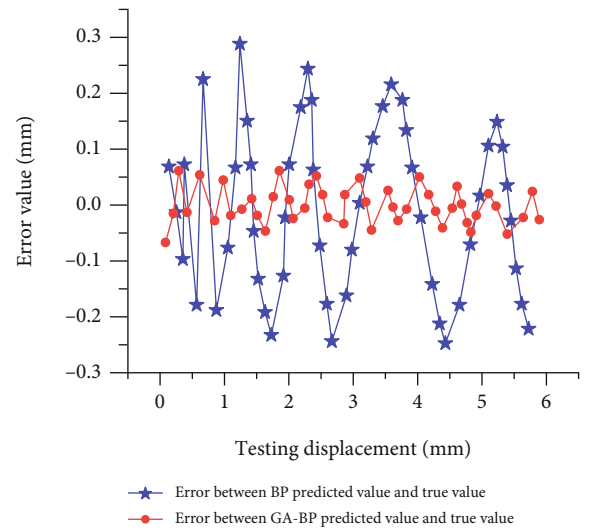

FIGURE 8: Comparison of traditional and optimized BP neural networks.

crossover method is applied, and the crossover operation equation of the l chromosome g_1 and the k chromosome g_k at the point i is as follows:

$$g_{li} = g_{li}(1 - a) + g_{ki}a, \tag{3}$$

$$g_{ki} = g_{ki}(1 - a) + g_{li}a, \tag{4}$$

where a is within $[0, 1]$. If the i gene of the j individual is selected for mutation processing, the operating equation is as follows:

$$g_{ij} = \begin{cases} g_{ij} + \left(g_{ij} - g_{\max}\right)Q(f), & \lambda > 0.5, \\ g_{ij} + \left(g_{\min} - g_{ij}\right)Q(f), & \lambda \leq 0.5, \end{cases} \tag{5}$$
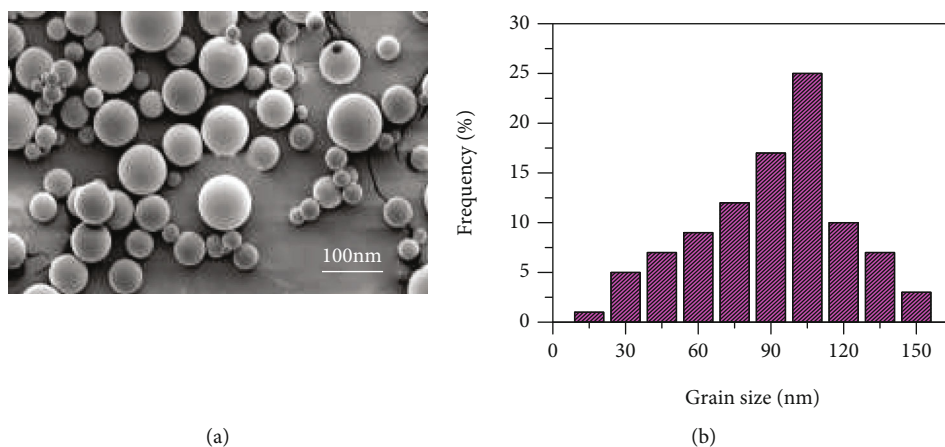
(a)

(b)

FIGURE 9: Morphology and particle size of silicon-coated fluorescent NPs. Note: (a) electron micrograph and (b) particle size distribution.
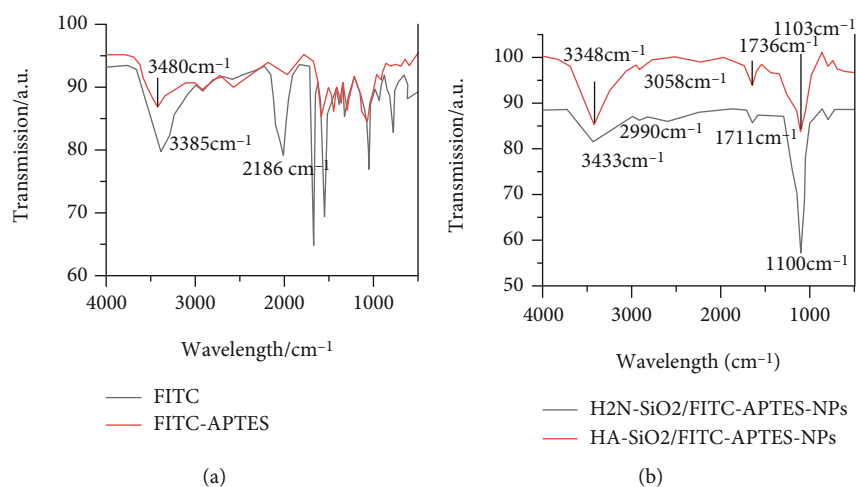

(a)

(b)

FIGURE 10: Infrared spectrum of modified electrode. Note: (a) infrared spectra of FITC and FITC-APTES precursors and (b) infrared spectra of H$_2$N-SiO$_2$/FITC-APTES-NPs and HA-SiO$_2$/FITC-APTES-NPs.

$$Q(f) = \lambda' \left(\frac{1-f}{F_{\max}} \right)^2, \tag{6}$$

where $g_{\max}$ is the maximum of g_{ij}, g_{ij} is the minimum, f is the number of iterations, $F_{\max}$ is the maximum number of evolutions, and λ and λ' are within $[0, 1]$.

The best optimized weight values are obtained by using GA methodology, and the weight and threshold values are optimized. It is further followed by the calculation of absolute values of residual, and then, the network weights are further modified. The accuracy requirements are then checked, and the entire optimization process of the BP neural network is then terminated.

2.3. The Fluorescent NPs Modified by HA

2.3.1. The Silicon-Coated Fluorescent NPs.
1.5 mg of fluorescein isothiocyanate (FITC) (Sigma-Aldrich, USA) is dissolved in 15 mL of double-distilled absolute ethanol, followed by ultrasound treatment. The solution is then dripped into anhydrous ethanol without distillation treatment, followed by magnetic stirring for 24 hours. Subsequently, the mixture is centrifuged and washed with anhydrous ethanol and n-hexanol alternately until there is no fluorescence in the supernatant. It is then dried in vacuum and stored in darkness [21]. 7.5 mL of cyclohexane, 2.5 mL of n-hexanol, and 1.88 mL of Triton x-100 are mixed uniformly, followed by magnetic stirring until it is clear. Subsequently, 250 μL of ultrapure water is added, followed by stirring for 15 min to form a relatively stable microemulsion system [22].

Figure 5 shows the preparation process of FITC-APTES. 0.25 mg of FITC and APTES (Sigma-Aldrich, USA) is dissolved in a mixture of 0.6 mL cyclohexane and 0.6 mL n-hexanol, followed by ultrasound treatment to fully dissolve them. The mixture is then dripped into the microemulsion system prepared above. After stirring for 30 min, nucleation occurs. 125 μL mixture of ethyl orthosilicate and 3-aminopropyltriethoxysilane is added [23], together with 50 μL ammonia water. After magnetic stirring for 24 h, a few drops of acetone are added to demulsify. Subsequently, the sample is washed alternately with absolute ethanol and
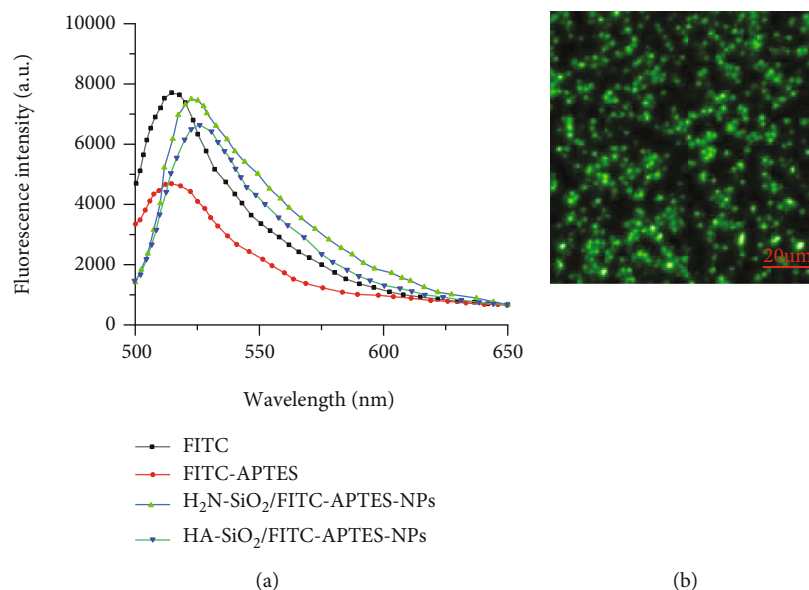
(a)

(b)

FIGURE 11: Fluorescence performance of silicon-coated fluorescent NPs. Note: (a) fluorescence spectra of FITC, FITC-APTES, H_2N-SiO_2/FITC-APTES-NPs, and HA-SiO_2/FITC-APTES-NPs and (b) fluorescence confocal microscopy image of HA-SiO_2/FITC-APTES-NPs.

ultrapure water [24]. Finally, H_2N-SiO_2/FITC-APTES-NPs are obtained and stored in refrigerator at 4°C for later use.

2.3.2. The HA Covalent Modification. 2.5 mg of sodium HA (NaA) is dissolved in 20 mL of ultrapure water by ultrasound treatment, with 0.02 mg of carbodiimide (EDC) and N-hydroxysuccinimide (NHS) (Ballingweier Reagent Company, China) added, respectively, followed by magnetic stirring for 2 h to activate the carboxyl group on HA [25]. 6 mL of the fluorescent NPs prepared above is then added, followed by stirring for 24 h under darkness. The ultrapure water is used for multiple washing. The unreacted HA and other small molecule impurities are removed through centrifugation [26]. Finally, HA covalently modified silicon-coated fluorescent NPs are obtained and stored at 4°C for later use.

2.3.3. Characterization and Determination of Silicon-Coated Fluorescent NPs. The electron microscope images of HN-SiO_2/FITC-APTES-NPs are measured using JEOL-2100 electron microscope (JEOL Company, Japan). A Nicolet Avatar 370 DTGS infrared spectrometer (Nicolet Avatar, USA) is used to obtain an infrared spectrum. The fluorescence spectrum is measured with Hitachi F-4600 fluorescence spectrophotometer (Hitachi, Japan) instrument. LSM 5 Pascal Laser Module laser scanning confocal microscope (Carl Zeiss, Germany) is used to characterize the results of cell incubation. A Bio-Rad Model 680 spectrophotometer (Bio-Rad Company, USA) is used to test the MTT results.

2.4. Cultivation and Survival Rate of Cancer Cells

2.4.1. Cultivation of Cancer Cells. Human cervical cancer Hela cells were cultured in DMEM containing 12% fetal bovine serum, penicillin, and streptomycin at 37°C [27]. Hela cells in the proliferation phase were treated with trypsinization and seeded (10^4-10^5 cells/well). 60 mg/L H_2N-SiO_2/FITC-APTES-NPs were then added to incubate the cells for
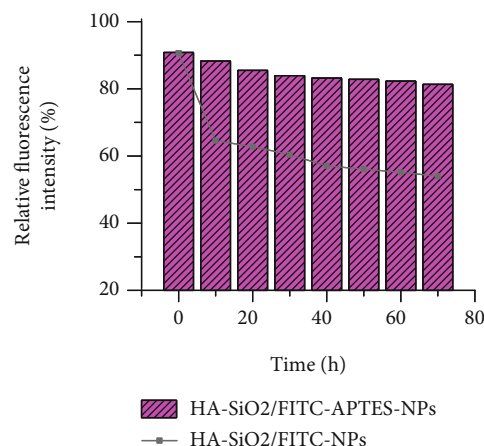

FIGURE 12: The dye leakage results.

4 h. After the supernatant was removed, the sample was rinsed with phosphate buffer and visualized using LSM 5 Pascal Laser Module laser scanning microscope.

2.4.2. The Survival Rate Detection. The H_2N-SiO_2/FITC-APTES-NPs were diluted using a phosphate buffer to configure solutions of 50, 100, 150, 200, 250, and 300 mg/mL, respectively. Hela cells were seeded at 10^4-10^5 cells/well in a 96-well plate, and the abovementioned different concentrations of phosphate buffer is then transferred to the 96-well plate, followed by incubation at 37°C overnight [28]. After the medium is removed, 10 μL of 1 mg/mL MTT (Sigma-Aldrich, USA) solution is added to each well to culture the cells for 4 hours, with the supernatant removed. 100 μL sodium dodecyl sulfate (SDS) was then added to each well to culture the cells for 15 minutes, so that the MTT can fully
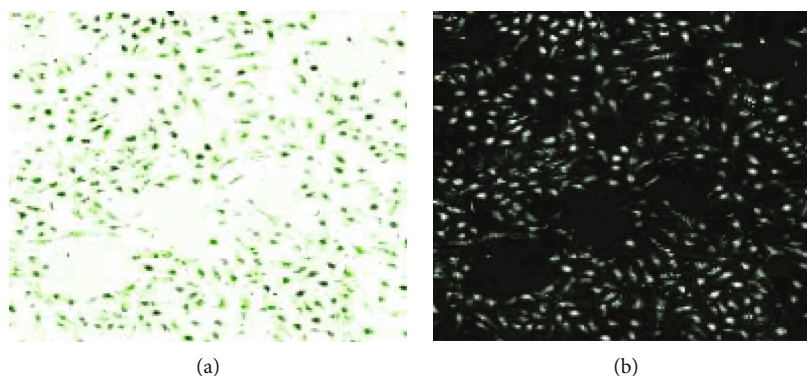
(a)

(b)

FIGURE 13: The fluorescence imaging of HA-SiO$_2$/FITC-APTES-NPs. Note: (a) bright-field fluorescence imaging and (b) dark-field fluorescence imaging.

react with the cells. The Bio-Rad Model 680 microplate reader is used to measure the absorbance at 580 nm.

2.5. *Statistics.* In this study, the data was processed by SPSS19.0, and all experimental data were expressed as mean ± standard deviation ($\bar{x} \pm s$). The root mean square (RMS) was applied to analyze the deviation between the predicted value and the expected value along with the evaluation of average absolute error (MAE). The *t*-test was used for comparison between groups. $P < 0.05$ was the threshold for significance.

3. Experimental Results

3.1. The BP Neural Network Optimized by GA

3.1.1. The Displacement Measurement. In the experiment of displacement measurement, the temperature in the control room is constant. The end surface of the probe and cellophane is wiped using alcohol to prevent dust and stains from affecting the measurement results. The angle between the probe and the target substance is 90°. Before the measurement, the laser is preheated. The probe fits closely to the aluminum workpiece surface, and the movement distance is controlled at 0.05 mm each time. The upper position machine is used to read the power value of the channels CH1 and CH2, and a curve is drawn to show the relationship between the displacement and the received power (Figure 6).

3.1.2. Comparative Analysis of Optimized GA-BP and Traditional BP Approach in Terms of Accuracy and Error Value. In the parameters of the BP neural network, 2 means input and 1 means output. 7 hidden layer nodes are set, and the target error is 0.0001. The number of training is 1500, and the training function is Trainingfu. The population size is set as 100 by GA, with a crossover probability of 0.2 and a mutation probability of 0.05. After setting of parameters, the power value and displacement value are used as the input and output of the neural network for repeated training, respectively. At the same time, the relevant parameters of the network are adjusted to make the training result reach the predicted value. To test the data, the electric displacement stage moves at 0.1 mm/step. The power meter is used
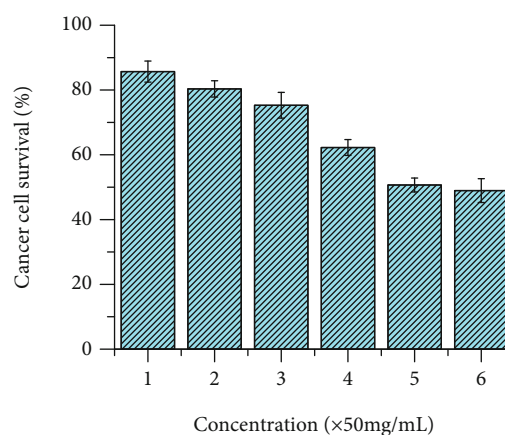

FIGURE 14: The relationship between cell survival rate and the concentration of HA-SiO$_2$/FITC-APTES-NPs.

to obtain the predicted output value and the predicted output value of the BP neural network optimized by GA.

Further, for evaluating the accuracy rates of traditional and optimized GA-BP-based approach, the accuracy parameters have been evaluated for the testing displacements.

From the graphical representation in Figure 7, it is depicted that the accuracy value increases with a small change in testing displacement for both the traditional and optimized cases. However, it should be noted that the value of accuracy for the optimized GA-BP neural network is much better compared to the traditional BP neural network-based approach. The final accuracy value obtained for the GA-BP method is 94.54% which is superior to the final accuracy value of 86.78% obtained for the traditional BP neural network method.

For the comparison of the traditional BP neural network and the GA optimized BP neural network, the RMS and MAE error values are introduced. It is found that the RMS and MAE of the optimized BP neural network are smaller, as shown in Figure 8.

Figure 8 depicts the error value with respect to testing displacement in (mm) for the normal BP predicted value and the true value. It also depicts the error rate between the GA-BP predicted values and the true values for the
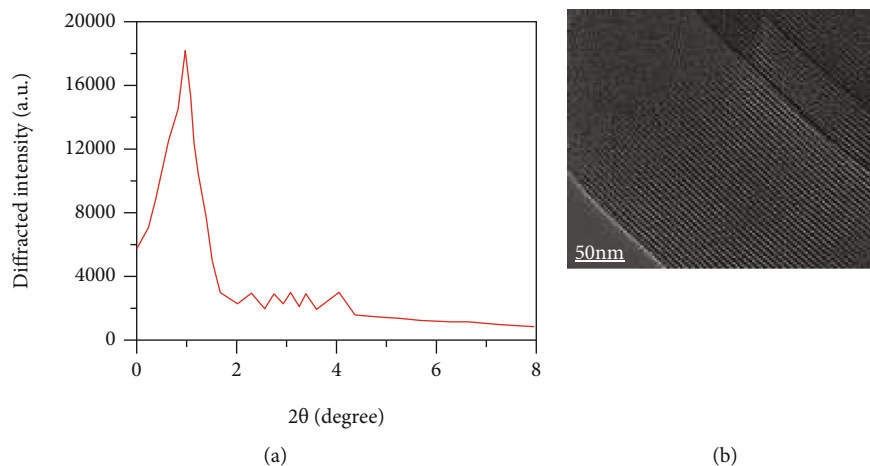
(a)

(b)

FIGURE 15: Characterization of CMK-2. Note: (a) diffraction image and (b) EMS.

GCE
CMK-2/GCE
Au NPs/CMK-2/GCE
Me-β-Cy/Au NPs/CMK-2/GCE

(a)

GCE
CMK-2/GCE
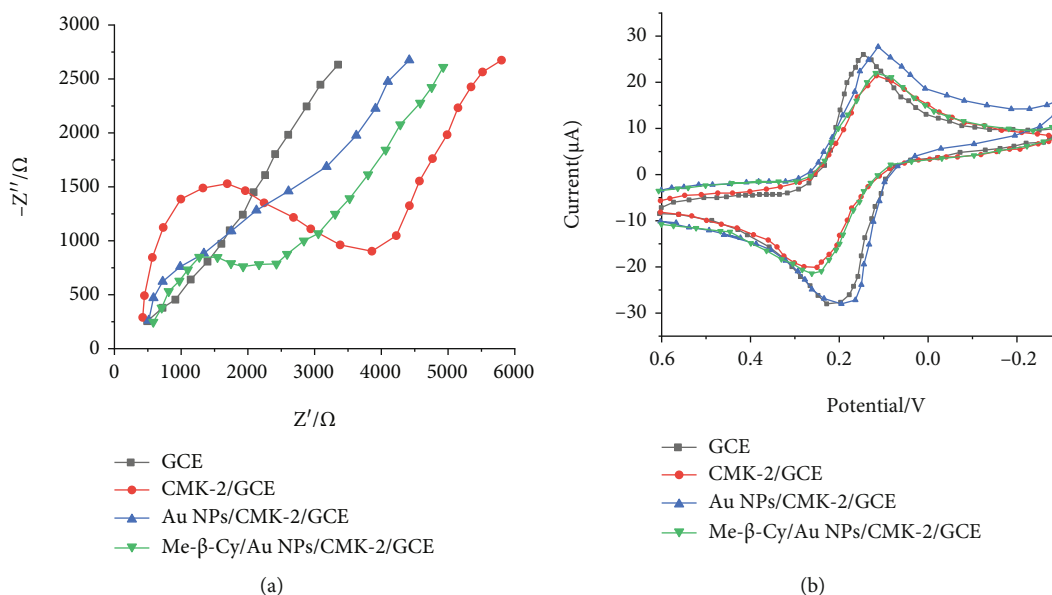Au NPs/CMK-2/GCE
Me-β-Cy/Au NPs/CMK-2/GCE

(b)

FIGURE 16: The electrochemical properties of the modified electrodes. (a) Electrochemical impedance curves. (b) CA spectra.

corresponding testing displacement. It can be seen that the error value is minimized near 0 for the case of the GA-BP-based approach which is not minimized much while utilizing the BP predictions alone. Also, it can be noted that the variations in the error values are minimized while utilizing the GA-based optimized BP neural network approach, as compared to the tradition BP neural network-based method.

3.2. Characterization of Silicon-Coated Fluorescent NPs

3.2.1. Morphology and Particle Size. It is evident from Figure 9(a) that the silicon-coated fluorescent NPs have good morphology, good dispersion, and relatively uniform particle size, which are sphere in shape. It is evident from Figure 9(b) that the particle size of NPs is about 105 nm.

3.2.2. The Infrared Spectrum. The infrared spectrum is obtained for measurement of FITC, FITC-APTES precursors, H_2N-SiO_2/FITC-APTES-NPs, and HA-SiO$_2$/FITC-

APTES-NPs. It is evident form Figure 10(a) that the FITC has the characteristic peak of the isothiocyano group at 2186 cm^{-1} where the FITC-APTES precursor does not possess the characteristic peak. It further indicates that a coupling reaction occurs between FITC and APTES, the isothiocyano group is combined with the guanidine group, and the FITC-APTES precursor is successfully prepared.

It is evident from Figure 10(b) that H_2N-SiO_2/FITC-APTES-NPs have the characteristic peak of amino group appears at 3433 cm^{-1}. The characteristic peak of silica at 1100 cm^{-1} shows that the prepared NPs contain amino groups. The HA-SiO$_2$/FITC-APTES-NPs have the stretching vibration peak of NH at 3058 cm^{-1}. The stretching vibration peak of CH is at 2990 cm^{-1}, and characteristic peaks of carboxyl groups are at 1711 cm^{-1} and 1736 cm^{-1}. These peaks are all caused by the group's stretching vibration, indicating that HA successfully binds to the surface of fluorescent NPs through amide bonds.

3.2.3. The Fluorescence Property. It is evident from Figure 11(a) that after FITC reacts with APTES to form the FITC-APTES precursor, the overall fluorescence intensity decreases. Though the fluorescence intensity of H_2N-SiO_2/FITC-APTES-NPs and HA-SiO_2/FITC-APTES-NPs decreases slightly, the peak value is still comparatively high. This indicates that the H_2N-SiO_2/FITC-APTES-NPs and HA-SiO_2/FITC-APTES-NPs have relatively good fluorescence properties. The fluorescence confocal microscopic image of HA-SiO_2/FITC-APTES-NPs shows that the fluorescence NPs are uniformly distributed (Figure 11(b)).

3.2.4. The Chemical Stability. Whether the formation of FITC-APTES will cause the leakage of fluorescent dyes is explored. The HA-SiO_2/FITC-APTES-NPs are immersed in ultrapure water for 80 h and compared with the HA-SiO_2/FITC-NPs for fluorescence intensity. It is found that the fluorescence intensity of HA-SiO_2/FITC-NPs decreases obviously in the first 10 hours, indicating that the dye leakage is serious. The curve gradually becomes stable after 10 hours. The fluorescence intensity of HA-SiO_2/FITC-APTES-NPs decreases slowly. The relative fluorescence intensity of HA-SiO_2/FITC-APTES-NPs in each time period higher than that of HA-SiO_2/FITC-NPs is maintained over 80% (Figure 12). It shows that the HA-SiO_2/FITC-APTES-NPs have good fluorescence stability.

3.2.5. Detection of Hela Tumor Cells. During diagnosis of tumor diseases, specific markers are often used as auxiliary means. HA can specifically recognize the unique HA adhesion factor protein receptor on the surface of cancer cells and binds to the surface of cancer cells. In this study, the HA-modified fluorescent NPs were visualized using a laser confocal microscope (Figure 13). The left was a bright-field optical image, and the right was a dark-field fluorescent image. The cells in the two corresponded to each other. In the fluorescence bright-field image, there was obvious green fluorescence on the surface of cancer cells, which indicated that HA-modified fluorescent NPs covered the surface of cancer cells (Figure 13(a)). In the dark-field image, the cells emitted bright green fluorescence (Figure 13(b)). Therefore, the HA-modified fluorescent NPs are a new method for early diagnosis of cancer cells.

3.2.6. Cell Survival Rate. In this study, the MTT method was used to determine the survival rate of cells. After MTT treatment of living cells, the mitochondrial-specific dehydrogenase in the cell would cause MTT to form water-insoluble blue-purple crystal formazan, which would not be formed in dead cells. To measure the absorbance of different concentrations of HA-modified fluorescent NPs at 580 nm, cells cultured in DMEM were set as blank group, and the cells cultured with fluorescent NPs were set as the control group. A lower survival rate indicates greater toxicity of HA-modified fluorescent NPs to cancer cells. It was found that as the concentration increased, the survival rate of cancer cells was gradually decreasing (Figure 14). To maintain good fluorescence intensity and cell survival rate, 50 mg/mL fluorescent NPs were selected for cell incubation experiments.
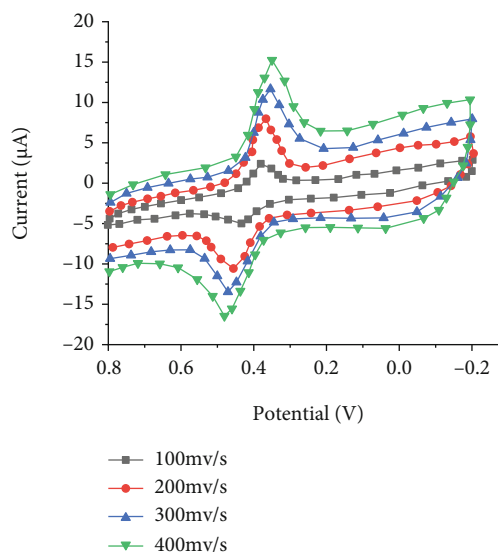

FIGURE 17: The CV spectra of Me-β-Cy/Au NPs/CMK-2/GCE at different scanning speeds.

3.3. The Characterization of the Modified Electrode

3.3.1. Characterization of CMK-2. The Rigaku Corporation SA-HF3 (Rigaku Corporation, Japan) is used to obtain the X-ray diffraction image of CMK-2. It is found that there is an obvious diffraction peak that appears at 2θ, indicating that CMK-2 has an obvious two-dimensional hexagonal structure (Figure 15(a)). The JEOL-2100 instrument (JEOL Company, Japan) is used to obtain the transmission EMS image of CMK-2. It is noted that it has a clear stripe structure and uniform size, indicating that the CMK-2 has a relatively good stripe structure (Figure 15(b)).

3.3.2. Electrochemical Properties of Modified Electrodes. Electrochemical impedance spectroscopy (EIS) can be used for the characterization of different electrodes. In this study, the impedance change during the modification of the electrode is explored, and further, the electrochemical impedance spectroscopy is observed. The electrochemical impedance of bare glass carbon electrode (GCE) CMK-2/GCE, Au NPs/CMK-2/GCE, and Me-β-Cy/Au NPs/CMK-2/GCE was measured in 1 mmol/L $Fe(CN)_6^{3-/4-}$ phosphate buffer (Figure 16(a)). The frequency change range is 0.01-10 kHz.

The electron transfer resistance of bare GCE is very small, about 500 Ω. After it is modified by CMK-2, the electron transfer resistance rapidly increases to 3800 Ω. The reason may be that the mesoporous silicon material itself does not conduct electricity. After electrodeposition Au, the impedance value is reduced, which shows that the Au NPs has good conductivity and promotes the transfer of $Fe(CN)_6^{3-/4-}$. After it is combined with Me-β-Cy, the electron transfer resistance continues to increase to 2100 Ω. It may be that the organic matter Me-β-Cy inhibits the transfer of $Fe(CN)_6^{3-/4-}$. Taken together, it can be confirmed that Me-β-Cy/Au NPs/CMK-2/GCE is successfully prepared in the study. Figure 16(b) shows the CV spectra of bare GCE, CMK-2/GCE, Au NPs/CMK-2/GCE, and Me-β-Cy/Au
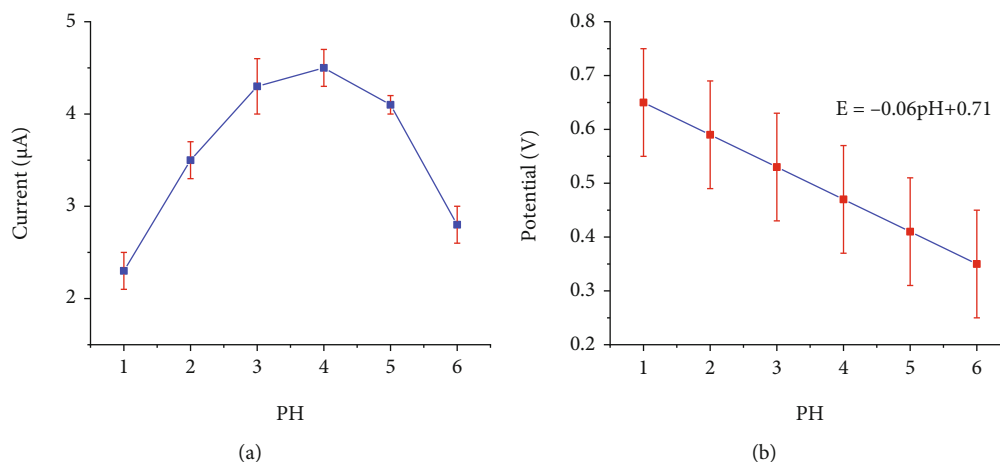
(a)

(b)

FIGURE 18: The influence of the pH value on modified electrode. Note: (a) the relationship curve between the peak current value and pH and (b) the linear correlation curve between reduction peak potential and pH of modified electrode.

NPs/CMK-2/GCE in 1 mmol/L $Fe(CN)_6^{3-/4-}$ phosphate buffer solution. The impedance changes in Figure 16(a) corresponded to that in Figure 16(b).

3.3.3. The Peak Current and Scanning Speed. Figure 17 shows the CA spectra of Me-β-Cy/Au NPs/CMK-2/GCE in a phosphate buffer at different scanning speeds. The scanning speed is controlled at 100-400 mv/s, and the results show that the scanning speed continues to increase providing the current peak value highest at 0.35 V.

3.3.4. The Optimal pH of the Solution. In this study, the influence of the pH value of the solution on the modified electrode is determined along with the relationship curve between the peak current value and pH drawn. The base solution is 15 μmol/L phosphate buffer with different pH levels. It is noted that as the pH value in the solution gradually increases from 1.0 to 4.0, the peak current signal also increases. When the pH value exceeds 4.0, the response signal decreases rapidly (Figure 18(a)). It may be that when the acidity of the solution increases, the number of protons is gradually decreasing, affecting the reaction on the electrode. When the pH is controlled in the range of 1.0-6.0, the reduction peak potential has a linear relationship with the pH value of the test solution. The slope of the fitting line is -60 mV, which is very close to the theoretical value -59 mV. It suggests that during the electrochemical reaction, the number of protons is equal to that of electrons (Figure 18(b)). When pH = 4.0, the peak current is the highest. Hence, pH = 4.0 was selected as the best pH value.

3.3.5. The Time for Modification. Me-β-Cy bonds to the gold NPs through S-Au bond, but this kind of covalent bond takes a certain time to achieve a stable state. Therefore, the time needed to reach a stable state is explored during Me-β-Cy modification. The reduction peak current in 15 μmol/L phosphate buffer is recorded with time, as shown in Figure 19.

The results show that when the modification time of Me-β-Cy is less than 15 h, the reduction peak current gradually
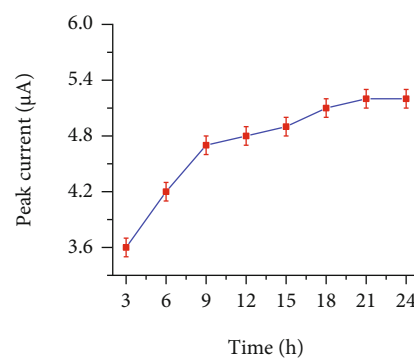

FIGURE 19: The reduction peak current with time.

increases with the time. After 15 h, the peak current tends to be stable. In this study, the modification time is set as 15 h.

4. Conclusion

In the study, the GA is used to optimize the BP neural network, and the identification NP sensor is used to diagnose cancer cells, aimed at realizing the early diagnosis of cancer cells by fluorescence imaging. The RMS and MAE of the optimized BP neural network are analyzed which were observed to be smaller than the traditional one. Furthermore, the modified electrode Me-β-Cy/Au NPs/CMK-2/GCE is successfully prepared and applied to the sensor. This sensor shows good stability, selectivity, and anti-interference property, providing a new method for the detection of early cancer cells. The prepared HA-modified fluorescent NPs have good fluorescence stability, and HA covalently modified fluorescent NPs can specifically bind to cancer cells. This method can be used in fluorescence imaging detection. This study provides a good theoretical basis for clinical diagnosis and prevention of cancer. However, the practical implementation of results using cervical cancer cells are universally applicable to other tumor cells, and its further verification will be the future research directions of this research work.

Data Availability

All data has been provided in the main manuscript.

Conflicts of Interest

The authors declare that they have no conflicts of interest.

References

[1] H. K. Jia, L. D. Yu, Y. Z. Jiang, H. N. Zhao, and J. M. Cao, "Compensation of rotary encoders using Fourier expansion-back propagation neural network optimized by genetic algorithm," *Sensors (Basel)*, vol. 20, no. 9, p. 2603, 2020.

[2] J. He, C. Pan, Y. Liu, and X. du, "Quantitative analysis of carbon with laser-induced breakdown spectroscopy (LIBS) using genetic algorithm and back propagation neural network models," *Applied Spectroscopy*, vol. 73, no. 6, pp. 678–686, 2019.

[3] J. Luo, R. Ren, and K. Guo, "The deformation monitoring of foundation pit by back propagation neural network and genetic algorithm and its application in geotechnical engineering," *PLoS One*, vol. 15, no. 7, article e0233398, 2020.

[4] Y. X. Hou, H. F. Zhao, Z. Zhang, and K. N. Wu, "A novel method for predicting cadmium concentration in rice grain using genetic algorithm and back-propagation neural network based on soil properties," *Environmental Science and Pollution Research International*, vol. 25, no. 35, pp. 35682–35692, 2018.

[5] Q. Li, H. Tao, J. Wang et al., "Warfarin maintenance dose prediction for patients undergoing heart valve replacement– a hybrid model with genetic algorithm and back-propagation neural network," *Scientific Reports*, vol. 8, no. 1, p. 9712, 2018.

[6] C. Huang, X. Jia, and Z. Zhang, "A modified back propagation artificial neural network model based on genetic algorithm to predict the flow behavior of 5754 aluminum alloy," *Materials (Basel)*, vol. 11, no. 5, p. 855, 2018.

[7] J. Shen, Y. Cui, J. Gu, Y. Li, and L. Li, "A genetic algorithm-back propagation artificial neural network model to quantify the affinity of flavonoids toward P-glycoprotein," *Combinatorial Chemistry & High Throughput Screening*, vol. 17, no. 2, pp. 162–172, 2014.

[8] P. He, Y. Fan, B. Pan, Y. Zhu, J. Liu, and D. Zhu, "Calibration and verification of dynamic particle flow parameters by the back-propagation neural network based on the genetic algorithm: recycled polyurethane powder," *Materials (Basel)*, vol. 12, no. 20, p. 3350, 2019.

[9] K. Shiba, R. Tamura, T. Sugiyama et al., "Functional nanoparticles-coated nanomechanical sensor arrays for machine learning-based quantitative odor analysis," *ACS Sens*, vol. 3, no. 8, pp. 1592–1600, 2018.

[10] M. Waldiya, D. Bhagat, N. R et al., "Development of highly sensitive H_2O_2 redox sensor from electrodeposited tellurium nanoparticles using ionic liquid," *Biosensors & Bioelectronics*, vol. 132, pp. 319–325, 2019.

[11] S. Wang, R. Farnood, and N. Yan, "Corn-derived dendrimer-like carbohydrate phytoglycogen nanoparticles as selective fluorescent sensor for silver ions," *Carbohydrate Polymers*, vol. 223, p. 115095, 2019.

[12] Y. T. Yaman, O. Akbal, and S. Abaci, "Development of clay-protein based composite nanoparticles modified single-used sensor platform for electrochemical cytosensing application," *Biosensors & Bioelectronics*, vol. 132, pp. 230–237, 2019.

[13] Y. Saylan, F. Yılmaz, A. Derazshamshir, E. Yılmaz, and A. Denizli, "Synthesis of hydrophobic nanoparticles for real-time lysozyme detection using surface plasmon resonance sensor," *Journal of Molecular Recognition*, vol. 30, no. 9, 2017.

[14] M. M. Rahman, J. Ahmed, and A. M. Asiri, "Thiourea sensor development based on hydrothermally prepared CMO nanoparticles for environmental safety," *Biosensors & Bioelectronics*, vol. 99, pp. 586–592, 2018.

[15] F. A. Ozdemir Olgun, A. Üzer, B. D. Ozturk, and R. Apak, "A novel cerium oxide nanoparticles-based colorimetric sensor using tetramethyl benzidine reagent for antioxidant activity assay," *Talanta*, vol. 182, pp. 55–61, 2018.

[16] H. Lu and S. Xu, "Visualizing BPA by molecularly imprinted ratiometric fluorescence sensor based on dual emission nanoparticles," *Biosensors & Bioelectronics*, vol. 92, pp. 147–153, 2017.

[17] Z. Khosroshahi, F. Karimzadeh, M. Kharaziha, and A. Allafchian, "A non-enzymatic sensor based on three-dimensional graphene foam decorated with Cu-xCu₂O nanoparticles for electrochemical detection of glucose and its application in human serum," *Materials Science & Engineering. C, Materials for Biological Applications*, vol. 108, p. 110216, 2020.

[18] Z. Yang, D. Y. Wang, Y. Pang et al., "Simultaneously detecting subtle and intensive human motions based on a silver nanoparticles bridged graphene strain sensor," *ACS Applied Materials & Interfaces*, vol. 10, no. 4, pp. 3948–3954, 2018.

[19] D. Li, S. Yu, C. Sun, C. Zou, H. Yu, and K. Xu, "U-shaped fiber-optic ATR sensor enhanced by silver nanoparticles for continuous glucose monitoring," *Biosensors & Bioelectronics*, vol. 72, pp. 370–375, 2015.

[20] J. S. Lee, B. Peng, A. C. Sabuncu et al., "Multiple consecutive recapture of rigid nanoparticles using a solid-state nanopore sensor," *Electrophoresis*, vol. 39, no. 5-6, pp. 833–843, 2018.

[21] F. Amiripour, S. N. Azizi, and S. Ghasemi, "Gold-copper bimetallic nanoparticles supported on nano P zeolite modified carbon paste electrode as an efficient electrocatalyst and sensitive sensor for determination of hydrazine," *Biosensors & Bioelectronics*, vol. 107, pp. 111–117, 2018.

[22] H. Wang, Y. Xie, S. Liu et al., "Presence of fluorescent carbon nanoparticles in baked lamb: their properties and potential application for sensors," *Journal of Agricultural and Food Chemistry*, vol. 65, no. 34, pp. 7553–7559, 2017.

[23] S. E. Jin, J. E. Jin, W. Hwang, and S. W. Hong, "Photocatalytic antibacterial application of zinc oxide nanoparticles and self-assembled networks under dual UV irradiation for enhanced disinfection," *International Journal of Nanomedicine*, vol. - Volume 14, pp. 1737–1751, 2019.

[24] S. Lotfi and H. Veisi, "Pd nanoparticles decorated /Fe₃O₄ nanocomposite modified glassy carbon electrode as a new electrochemical sensor for simultaneous determination of acetaminophen and phenylephrine," *Materials Science & Engineering. C, Materials for Biological Applications*, vol. 105, p. 110112, 2019.

[25] D. Refaat, M. G. Aggour, A. A. Farghali et al., "Strategies for molecular imprinting and the evolution of MIP nanoparticles as plastic antibodies-synthesis and applications," *International Journal of Molecular Sciences*, vol. 20, no. 24, p. 6304, 2019.

[26] X. Jin, G. Fang, M. Pan, Y. Yang, X. Bai, and S. Wang, "A molecularly imprinted electrochemiluminescence sensor based on upconversion nanoparticles enhanced by electrodeposited rGO for selective and ultrasensitive detection of

clenbuterol," *Biosensors & Bioelectronics*, vol. 102, pp. 357–364, 2018.

[27] Z. Q. Zheng, J. D. Yao, B. Wang, and G. W. Yang, "Light-controlling, flexible and transparent ethanol gas sensor based on ZnO nanoparticles for wearable devices," *Scientific Reports*, vol. 5, no. 1, 2015.

[28] H. Shibata, Y. Ikeda, and D. Citterio, "Inkjet-printed colorimetric paper-based gas sensor arrays for the discrimination of volatile primary amines with amine-responsive dye-encapsulating polymer nanoparticles," *Methods in Molecular Biology*, vol. 2027, pp. 101–114, 2019.